ACS Photonics
Article
pubs.acs.org/journal/apchd5

Analytical Modeling of Graphene Plasmons

Renwen Yu,[†] Joel D. Cox,[†] J. R. M. Saavedra,[†] and F. Javier García de Abajo*[,†,‡]

[†]ICFO-Institut de Ciencies Fotoniques, The Barcelona Institute of Science and Technology, 08860 Castelldefels (Barcelona), Spain
[‡]ICREA-Institució Catalana de Recerca i Estudis Avançats, Passeig Lluís Companys 23, 08010 Barcelona, Spain

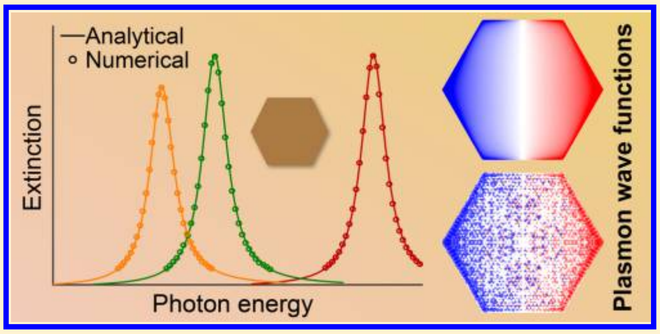

ABSTRACT: The two-dimensionality of graphene and other layered materials can be exploited to simplify the theoretical description of their plasmonic and polaritonic modes. We present an analytical theory that allows us to simulate these excitations in laterally patterned structures in terms of plasmon wave functions (PWFs). Closed-form expressions are offered for their associated extinction spectra, involving only two real parameters for each plasmon mode and graphene morphology, which we calculate and tabulate once and for all. Classical and quantum-mechanical formulations of this PWF formalism are introduced, in excellent mutual agreement for armchaired islands with >10 nm characteristic size. Examples of application are presented to predict both plasmon-induced transparency in interacting nanoribbons and excellent sensing capabilities through the response to the dielectric environment. We argue that the PWF formalism has general applicability and allows us to analytically describe a wide range of 2D polaritonic behavior, thus providing a convenient tool for the design of actual devices.

KEYWORDS: *graphene plasmons, 2D polaritonics, electromagnetic modeling, plasmon wave function, plasmon-induced transparency, optical sensing*

Plasmons are collective oscillations of conduction electrons found in different materials, where they interact strongly with light and can confine it down to nanoscale spatial regions to generate enormous optical field intensity enhancement.[1] These extraordinary properties are of paramount importance for a wide range of applications, such as optical sensing and modulation,[2−6] the enhancement of nonlinear optical processes,[7,8] photocatalysis,[9−14] and photothermal therapies.[15,16] In these applications, precise spectral positioning of plasmon resonances is needed to achieve optimal performance. This is commonly accomplished by fabricating noble metal nanostructures with specific sizes and morphologies. However, despite being the workhorse of plasmonics research, noble metals unfortunately present relatively large inelastic losses, thus limiting plasmon lifetimes in metallic nanostructures[17] and leading to a severe reduction in optical confinement. Additionally, the large number of electrons involved in the plasmons of metallic nanostructures limits the ways in which we can influence them in a dynamical fashion.

Recently, highly doped graphene has emerged as an outstanding plasmonic material[18−31] that simultaneously provides strong field confinement with relatively lower loss.[32] More importantly, plasmons in graphene are sustained by a small number of charge carriers compared to those of traditional noble metals, a property that makes them amenable to display new phenomena, including an unprecedented electro-optical response. Indeed, active tunability of the plasmon resonance frequency has been achieved via electrical gating.[21−26,28−30] Additionally, several of the aforementioned applications that were first realized using noble metal plasmons have now been demonstrated using a tunable graphene platform.[31−34] However, the design of graphene-based plasmonic devices requires accurate modeling of their optical response, often necessitating time-consuming numerical simulations.

Here we present an analytical model based on the so-called plasmon wave functions (PWFs), which can accurately predict the optical response associated with plasmonic resonances sustained in doped graphene structures with arbitrary shape and size. Actually, the present model can describe plasmons in any two-dimensional (2D) structure (in particular using only two real-valued parameters per plasmon to model far-field scattering) and thus constitutes a powerful tool for the design of graphene-based nanoplasmonic devices. We further compare the concept of the PWFs, which are the induced charge density profiles associated with confined plasmonic modes, with rigorous classical electromagnetic and atomistic quantum-mechanical (QM) models for nanostructured graphene. As a proof-of-concept, we demonstrate the use of our analytical model in the study of various applications for graphene-based nanostructures, namely, plasmon-induced transparency and refractive index sensing.

Special Issue: 2D Materials for Nanophotonics

Received: July 9, 2017
Published: July 31, 2017

DOI: 10.1021/acsphotonics.7b00740
ACS Photonics 2017, 4, 3106−3114

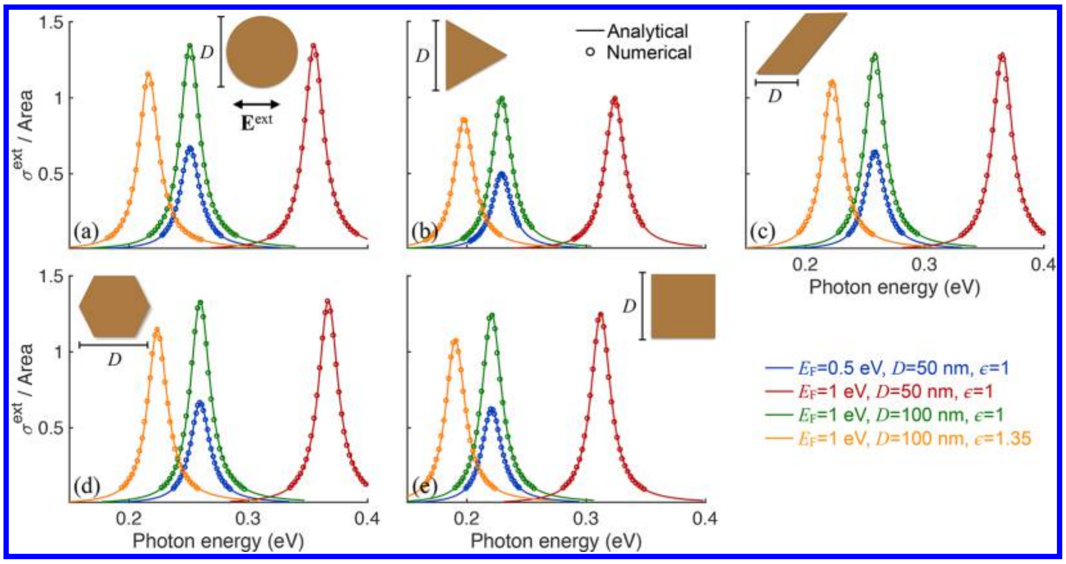

Figure 1. Analytical description of plasmons in graphene islands of different morphology. We present the extinction cross-section for (a) disks, (b) triangles, (c) ribbons, (d) hexagons, and (e) squares. In each figure, analytical results obtained using the plasmon wave function (PWF) of the lowest-order dipolar mode (solid curves) are compared with numerical simulations (symbols) for different combinations of characteristic size D, graphene Fermi energy E_F, and surrounding dielectric permittivity ϵ (see color-coded legend). In all calculations we describe the graphene surface conductivity using the Drude model (eq 2), adopting a phenomenological inelastic damping energy $\hbar\tau^{-1}$ = 20 meV (i.e., $\tau \approx 33$ fs) and considering normally impinging light polarized in the direction indicated in the inset of panel (a).

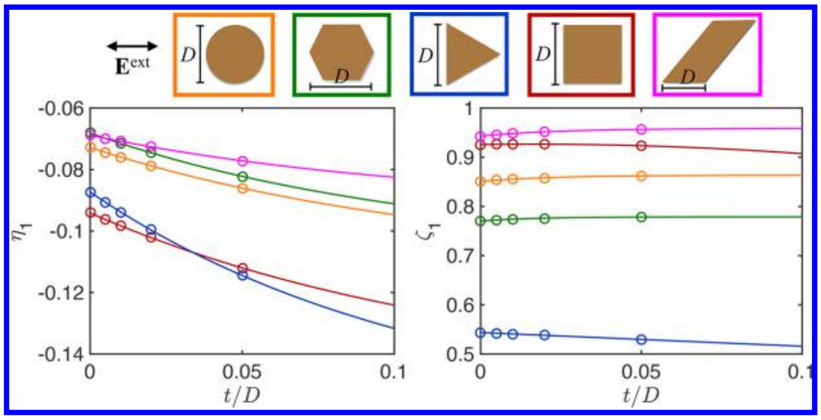

Figure 2. Thickness dependence of the PWF analytical parameters. We present the eigenvalue η_1 and normalized dipole moment ζ_1 for the lowest-order dipolar plasmon mode of disks, hexagons, triangles, squares, and ribbons (see symbols, which are color-coded with the borders of the upper inset figures) as a function of the normalized effective graphene thickness t/D, where the characteristic size D of a structure is indicated in the upper insets along with the light polarization direction (double arrow). Symbols for η_1 are obtained by fitting the numerically computed extinction spectra in the electrostatic limit, while ζ_1 is calculated using eq 10. Solid curves, color-coded to the borders of the upper inset figures, correspond to the fitted expressions provided in Table 1.

■ RESULTS AND DISCUSSION

Classical PWFs in Different Morphologies. The optical response of graphene nanoislands is well-described in the electrostatic limit, as their plasmon resonances typically appear in the infrared regime, where the light wavelength is much larger than the plasmon wavelength of the material.[35,36] In previous studies, an eigenmode expansion method has been adopted to express the linear optical response of a graphene nanostructure in terms of its supported plasmon modes.[35,36] Alternatively, one can associate a plasmon mode j with its induced charge distribution, which we refer to as the PWF of mode j.[37] We demonstrate the power of the PWF formalism in Figure 1. In the spectral region dominated by the lowest-order plasmon mode (j = 1) supported by graphene islands of varied morphology, we compare extinction spectra predicted in the analytical PWF description (solid curves, details in Methods) with those obtained upon fully numerical finite-element solution of Maxwell's equations (dashed curves, COMSOL). We find excellent agreement among analytical and numerical results, regardless of the nanostructure characteristic size D, graphene Fermi energy E_F, or dielectric permittivity of the surrounding environment ϵ (see colored labels). Here and in what follows, we describe the graphene surface conductivity in the Drude approximation, adopting a phenomenological inelastic damping rate $\hbar\tau^{-1}$ = 20 meV (i.e., $\tau \approx 33$ fs; see Methods), unless specified otherwise.

The analytical model used to produce the results presented in Figure 1 is based on two parameters: the plasmon mode eigenvalue η_j and dipole moment ζ_j, where j is a mode index, and in this figure we focus on j = 1, the lowest-order plasmon supported by each of the graphene islands under consideration. These two parameters are independent of the material properties, and in fact, they are determined by geometrical features alone. This means that the PWF treatment can also be used to describe other nanostructured 2D materials characterized by an isotropic surface conductivity. More precisely, the eigenvalue η_j corresponds to the resonant value of the quantity $\eta = \mathrm{i}\sigma(\omega)/D\omega\epsilon$, where $\sigma(\omega)$ is the graphene conductivity, ω is the optical frequency, D is a characteristic size of the structure (see insets in Figure 1), and ϵ is the permittivity of the dielectric environment. Using the Drude model for the graphene conductivity (eq 2 in Methods), the plasmon frequency of mode j can be analytically resolved in terms of the eigenvalue as[36] $\omega \approx \omega_j - \mathrm{i}\tau^{-1}/2$ with

$$\omega_j = \frac{e/\hbar}{\sqrt{-\pi\eta_j\epsilon}}\sqrt{\frac{E_\mathrm{F}}{D}} \tag{1}$$

Plasmons are then associated with negative eigenvalues $\eta_j < 0$. This expression explains why the analytical model undergoes a small redshift of the plasmon resonance peaks in all cases considered in Figure 1 when the average surrounding permittivity ϵ increases from 1 to 1.35. We note that according to eq 1 the resonance positions for structures with the same value of $\sqrt{E_\mathrm{F}/D\epsilon}$ should coincide, as illustrated by the green and blue curves.

The results of Figure 1 correspond to islands of zero thickness. However, the charge that is optically induced on the graphene as the result of the excitation of a plasmon spans a finite thickness determined by the spatial extension of the out-of-plane carbon 2p orbitals. A value of ~0.34 nm is typical used, corresponding to the interplane distance in graphite. Although this is an *ad hoc* parameter, it has been used in many prior studies of graphene plasmonics. Then, the thickness of the island t has a finite value that can influence the plasmons. We thus present in Figure 2 the dependence of the eigenvalue and dipole-moment parameters on the normalized thickness t/D. We find that the mode eigenvalue, which determines the plasmon resonance frequency, is more sensitive to variations of t/D, while the mode dipole moment ζ_1 is relatively robust. We thus conclude that the spectral position of a plasmon resonance predicted for a graphene nanostructure described with a nonzero thickness is more prone to inaccuracy, unless a proper treatment of the thickness parameter is performed. Incidentally, the mode eigenvalues η_1 are obtained by fitting numerically computed extinction spectra in the electrostatic limit for the lowest-order plasmon mode, while ζ_1 is calculated using eq 10 (see Methods). We also provide t/D-dependent fits (solid curves in Figure 2) in Table 1.

Table 1. Fitting Functions for $\eta_1 = a_\eta \exp(b_\eta x) + c_\eta$ and $\zeta_1 = a_\zeta \exp(b_\zeta x) + c_\zeta$ Corresponding to Graphene Islands of Different Morphologies as a Function of the Normalized Thickness $x = t/D$[a]

	disk	hexagon	triangle	square	ribbon
a_η	0.03801	0.03846	0.07418	0.05537	0.02326
b_η	−8.569	−9.105	−9.106	−7.795	−8.878
c_η	−0.1108	−0.1066	−0.1615	−0.1495	−0.09208
a_ζ	−0.01267	−0.008482	1	−2.752	−0.01572
b_ζ	−45.34	−62.02	−0.2826	0.09027	−39.21
c_ζ	0.8635	0.7787	−0.4563	0.9258	0.9588

[a] We apply these expressions for all morphologies considered in Figure 2 except the graphene square, for which we have $\zeta_1 = a_\zeta x^2 + b_\zeta x + c_\zeta$.

Quantum-Mechanical PWFs. We present in Figure 3 the spatial distributions of PWFs $\rho_1(\vec{\theta})$ as a function of the normalized in-plane position vector $\vec{\theta} \equiv \mathbf{R}/D$ corresponding to the lowest-order plasmon mode contained in the collection of graphene structures considered here. In the upper row of Figure 3a, we present PWFs obtained using the classical model, with blue and red colors representing charges of opposite sign, so that the charge neutrality condition $\int d^2\vec{\theta}\ \rho_1(\vec{\theta}) = 0$ is evident upon inspection. For comparison, the induced charge distributions of the same modes obtained from an atomistic QM model for graphene islands with lateral sizes on the order of ~10 nm are presented in the lower row of Figure 3a (see Methods for details on the QM model). We denote these induced charges associated with the plasmons as quantum PWFs (see Methods). The similarity between PWFs obtained from the classical and quantum models clearly indicates that the concept also holds in the quantum regime. In Figure 3b, PWFs for the first three lowest-order plasmon modes ($j = 1-3$, see labels) are shown for a 1D graphene nanoribbon, where the $j = 2$ mode, yielding $\zeta_2 = 0$, is a dark plasmon.

Quantum PWFs are useful for studying the interaction between different graphene structures, avoiding costly numerical simulations. We put this concept to the test in Figure 4, where we present results for two parallel ribbons with a small vertical separation between them. In particular, we plot the extinction cross-section for transversal light polarization. The spectra are dominated by the lowest-order ribbon plasmon, which splits into two hybridized plasmons, one of which is dipole-active (i.e., it shows up in the spectra) and moves to the blue as the distance between ribbbons is decreased. The agreement between fully atomistic QM simulations (solid curves) and the quantum-PWF model (eq 13, broken curves) is rather satisfactory.

Plasmon-Induced Transparency. As a way to demonstrate the versatility of the PWF formalism, we study the optical response of graphene structures interacting with external elements or with one another (see details in Methods). In Figure 5a we first present the optical extinction spectra of isolated graphene nanoribbons with different widths D, both of which are doped to $E_\mathrm{F} = 1$ eV, and we include modes up to $j \leq 3$ (see Figure 3b). In the frequency range shown, a prominent peak associated with the $j = 1$ dipolar mode supported in the smaller ribbon ($D = 22$ nm, blue curves) appears around 0.55 eV, whereas the extinction from the larger ribbon ($D = 51$ nm, red curves) is negligible at that energy. However, as shown in Figure 5b, where we simulate the decay rate of a quantum emitter with transition dipole $\mathbf{p}^\mathrm{ext}$ in the presence of either ribbon, a resonance feature appears in the spectrum for the larger one, which corresponds to its $j = 2$ dark mode. This dark mode plays an important role when considering the optical response of a dimer formed by the coplanar combination of the two ribbons, with an edge-to-edge separation distance d, as shown in Figure 5c. The interaction between the bright and dark plasmonic modes in the small and large ribbons, respectively, results in a transparency window appearing around 0.55 eV, which becomes more pronounced as the separation distance decreases from $d = 50$ nm to $d = 3$ nm. This phenomenon is known as plasmon-induced transparency and has several applications, including slow light generation.[38,39] We note that results based on the PWF formalism are found to be in excellent agreement with fully numerical simulations.

Sensing of the Dielectric Environment. As another proof-of-concept demonstration, we apply the PWF formalism

DOI: 10.1021/acsphotonics.7b00740
ACS Photonics 2017, 4, 3106−3114

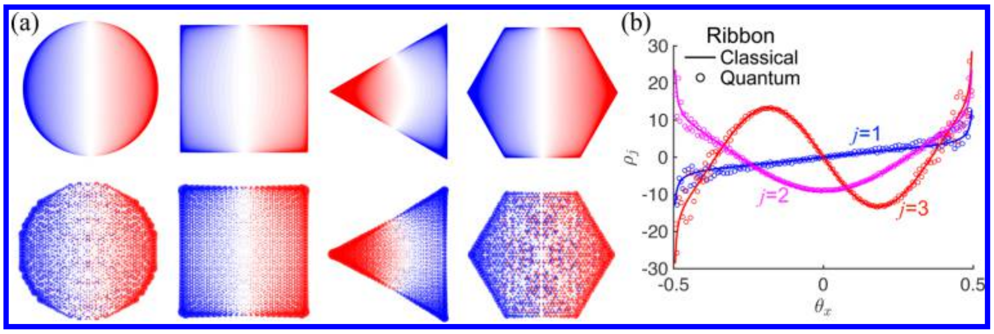

Figure 3. Classical vs quantum PWFs. (a) Density plots of the PWFs for the lowest-order ($j = 1$) dipole mode are presented in the top row for several graphene geometries using the classical quasistatic model, whereas in the bottom row we show the induced charge distributions at the spectral position of the lowest-order plasmon resonance computed using an atomistic QM model (see Methods). Blue and red colors represent charges of opposite signs. (b) PWFs of the first three lowest-order ($j = 1-3$, see labels) plasmon modes in graphene ribbons along the transversal ribbon direction x are obtained using the classical model (solid curves). The induced charge distribution from the QM model is presented as symbols. The orientation of the incident light is along the ribbon width. In the quantum calculations we take $D = 10$, 8.8, 15, 10, and 20 nm for the disk, square, triangle, hexagon, and ribbon, respectively (see upper insets of Figure 2). These values correspond to ~2000−3000 carbon atoms for the finite islands.

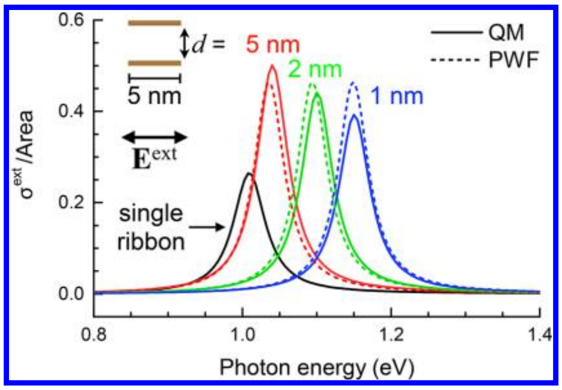

Figure 4. Description of interacting nanoribbon plasmons using quantum-mechanical PWFs. We compare the absorption cross-section of two vertically offset nanoribons (5 nm width) for different separations d (see color-coded labels) as described by direct QM simulations of the combined structure (solid curves) and using atomistic PWFs (dashed curves). Ribbons have armchair edges, and their Fermi and damping energies are $E_F = 1$ eV and $\hbar\tau^{-1} = 50$ meV, respectively.

to simulate refractive index sensing assisted by mid-infrared plasmons in graphene nanostructures. In particular, we study in Figure 6a,b the optical response of graphene disks ($E_F = 0.35$ eV, $D = 120$ nm) and ribbons ($E_F = 0.35$ eV, $D = 125$ nm), respectively, when they are immersed in media characterized by different values of the refractive index $n = \sqrt{\epsilon}$. Here we adopt the local random-phase approximation (local-RPA) model for the graphene conductivity to properly account for the interband contribution to the optical response (see Methods), and we consider two different values of the phenomenological inelastic damping energy width, $\hbar\tau^{-1} = 1$ and 10 meV, corresponding to the results plotted as solid and dashed curves, respectively. In order to quantify the performance of the proposed sensor, we introduce the parameter $S \equiv \Delta\lambda/\Delta n$, which indicates the resonance wavelength shift per refractive index unit (RIU) change. From Figure 6c,d, we observe that both graphene disks and ribbons yield similar shifts of ~9 μm/RIU, independent of the chosen inelastic damping rate. The bulk figure of merit is defined as FoM = S/fwhm, where fwhm denotes the full width at half-maximum of the resonance. We find a fwhm ≈ 79 nm (770 nm) for $\hbar\tau^{-1} = 1$ meV (10 meV) from Figure 6a,b, which gives a bulk FoM ≈ 113.9 (11.7). Note that the bulk FoMs calculated using either inelastic damping rate provide large values compared to others found in the literature.[40,41]

CONCLUSION

In brief, this paper demonstrates the versatility of plasmon wave functions for studying the optical response of graphene structures with arbitrary morphologies. The present model is analytical and characterizes a far-field plasmon resonance in a given geometry using only two real-valued parameters. The spatial distribution of PWFs calculated from classical modeling is found to be in excellent agreement with those obtained from atomistic quantum-mechanical simulations, even for structures of small (~10 nm) lateral size when the edges are armchaired. We apply our analytical model to the study of graphene ribbon dimers, which accurately describes the plasmon-induced transparency that arises when bright and dark modes couple strongly. Additionally, the PWF formalism is used to explore graphene plasmon-assisted refractive index sensing at mid-infrared frequencies, for which we predict a large bulk FoM (around 114), even when considering a conservative high inelastic damping rate. Finally, we note that the present analytical PWF formalism is universal and can be applied to model the optical response of other two-dimensional materials or thin films using their local 2D conductivitites as input.

METHODS

Graphene Conductivity. In our classical approach, we characterize graphene through its optical surface conductivity, which is given in the local limit of the random-phase approximation by[36,42]

$$\sigma_{\text{local-RPA}}(\omega) = \frac{e^2}{\pi\hbar^2}\frac{\mathrm{i}}{\omega + \mathrm{i}\tau^{-1}} \times\left[\mu^T - \int_0^\infty \mathrm{d}E \frac{f(E) - f(-E)}{1 - 4E^2/[\hbar^2(\omega + \mathrm{i}\tau^{-1})^2]}\right]$$

In the above expression $\mu^T = \mu + 2k_BT\log(1 + \mathrm{e}^{-\mu/k_BT})$ is the thermally corrected chemical potential, μ is the actual temperature-dependent chemical potential, τ is the inelastic relaxation time, and $f(E) = 1/[1 + \mathrm{e}^{(E-\mu)/k_BT}]$. Analytical expressions for μ have been reported elsewhere,[43] where it is

DOI: 10.1021/acsphotonics.7b00740
ACS Photonics 2017, 4, 3106−3114

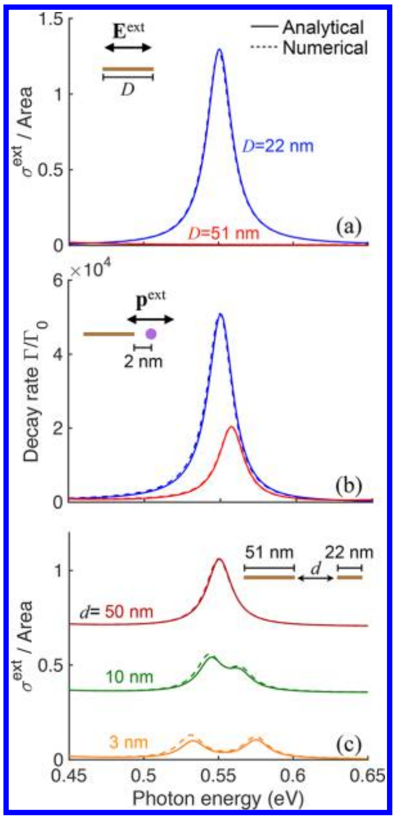

Figure 5. Plasmon-induced transparency in paired graphene ribbons. (a) Optical response of individual graphene ribbons of widths $D = 22$ nm (blue curves) and 51 nm (red curves) under normal incidence with light polarization across the width of the ribbon. We assume $E_F = 1$ eV in all cases. The peak in extinction around 0.55 eV corresponds to the lowest-order plasmon mode in the smaller ribbon, while the contribution from the larger ribbon is negligible in the photon energy range under examination. (b) Decay-rate enhancement for an external unit dipole $\mathbf{p}^{ext}$ placed 2 nm away from the edge of the ribbons considered in panel (a). The dipole is oriented along the ribbon width. (c) Optical response of dimers composed of the two ribbons presented in panel (a) separated by an edge-to-edge distance d in a coplanar configuration. When the separation distance d decreases from 50 nm to 3 nm (see labels), a transparency window appears around 0.55 eV in the extinciton spectra as a result of the interaction between the $j = 1$ mode (lowest-order dipole mode) in the smaller ribbon and the $j = 2$ mode (first dark mode) in the larger one. Our PWF-based analytical results (solid curves) agree well with numerical simulations (broken curves) in all cases.

shown that $\mu = \sqrt{\sqrt{(E_F)^4 + B^2(k_BT)^4} - B(k_BT)^2}$ with $B = \ln^2(16)/2 \approx 3.84$ constitutes a good analytical approximation that reduces to $\mu \approx E_F$ in the $E_F \gg k_BT$ limit. Notice that from an experimental viewpoint the doping conditions determine a temperature-independent carrier density n, which in turns controls the Fermi energy $E_F = \hbar v_F\sqrt{\pi n}$ (i.e., the chemical potential at zero temperature), where $v_F \approx 10^6$ m/s is the Fermi velocity in graphene. The local-RPA conductivity includes effects due to finite temperature, as well as both intra- and interband electron−hole pair transitions in graphene. However, for high doping at room temperature and frequencies well below $2E_F$, one can safely neglect temperature and interband effects, so that the expression above reduces to the Drude conductivity model,

$$\sigma_D(\omega) = \frac{e^2}{\pi\hbar^2}\frac{iE_F}{\omega + i\tau^{-1}} \tag{2}$$

Throughout this work, we adopt both Drude and local-RPA conductivities, assuming $T = 300$ K in cases where the latter is used.

Classical Eigenmode Expansion and PWFs. Following the formalism presented in refs 35 and 37 we intend to find the electric field $\mathbf{E}$ produced by a planar graphene structure in response to an impinging field $\mathbf{E}^{ext}$, expressing it in frequency domain ω as the solution of the self-consistent equation

$$\mathbf{E}(\mathbf{R}, \omega) = \mathbf{E}^{ext}(\mathbf{R}, \omega) + \frac{i\sigma(\omega)}{\omega\epsilon(\omega)}\nabla_{\mathbf{R}}\int\frac{d^2\mathbf{R}'}{|\mathbf{R} - \mathbf{R}'|}\nabla_{\mathbf{R}'}\cdot f(\mathbf{R}')\,\mathbf{E}(\mathbf{R}', \omega) \tag{3}$$

Here, $\epsilon(\omega)$ is the average permittivity of the materials on either side of the graphene plane, while $f(\mathbf{R})$ is a filling function that is 1 when the in-plane 2D position vector $\mathbf{R}$ lies within the graphene structure and 0 elsewhere (a vanishing positive number in practice). It should be noted that we are formulating the self-consistent electric field $\mathbf{E}$ in the graphene plane and the surface conductivity σ can be computed using either Drude or local-RPA models. Defining the normalized 2D in-plane vectors $\vec{\theta} \equiv \mathbf{R}/D$ and $\vec{\mathcal{E}}(\vec{\theta}, \omega) \equiv D\sqrt{f(\vec{\theta})}\,\mathbf{E}(\vec{\theta}, \omega)$, where D is a characteristic length of the geometry under consideration (e.g., the side length of the graphene island), eq 3 can be recast as

$$\vec{\mathcal{E}}(\vec{\theta}, \omega) = \vec{\mathcal{E}}^{ext}(\vec{\theta}, \omega) + \eta(\omega)\int d^2\vec{\theta}'\,\mathbf{M}(\vec{\theta}, \vec{\theta}')\cdot\vec{\mathcal{E}}(\vec{\theta}', \omega) \tag{4}$$

where $\eta(\omega) = i\sigma(\omega)/(\omega D\epsilon)$ and

$$\mathbf{M}(\vec{\theta}, \vec{\theta}') = \sqrt{f(\vec{\theta})\,f(\vec{\theta}')}\,\nabla_{\vec{\theta}} \otimes \nabla_{\vec{\theta}}\frac{1}{|\vec{\theta} - \vec{\theta}'|}$$

is a real and symmetric operator. In consequence, $\mathbf{M}$ admits a set of real eigenmodes $\vec{\mathcal{E}}_j(\vec{\theta})$ and eigenvalues $1/\eta_j$ defined through

$$\vec{\mathcal{E}}_j(\vec{\theta}) = \eta_j\int d^2\vec{\theta}'\,\mathbf{M}(\vec{\theta}, \vec{\theta}')\cdot\vec{\mathcal{E}}_j(\vec{\theta}') \tag{5}$$

such that the eigenmodes satisfy the orthogonality condition

$$\int d^2\vec{\theta}\,\vec{\mathcal{E}}_j(\vec{\theta})\cdot\vec{\mathcal{E}}_{j'}(\vec{\theta}) = \delta_{jj'} \tag{6}$$

and the closure relation

$$\sum_j \vec{\mathcal{E}}_j(\vec{\theta}) \otimes \vec{\mathcal{E}}_j(\vec{\theta}') = \delta(\vec{\theta} - \vec{\theta}')\mathbb{I}_2$$

where $\mathbb{I}_2$ denotes the 2×2 identity matrix in the subspace of quasistatic electric-field modes. Using the above eigenmodes, we write the solution to eq 4 as

$$\vec{\mathcal{E}}(\vec{\theta}, \omega) = \sum_j \frac{C_j}{1 - \eta(\omega)/\eta_j}\vec{\mathcal{E}}_j(\vec{\theta})$$

where the expansion coefficients are given by

$$C_j = \int d^2\vec{\theta}\,\vec{\mathcal{E}}_j(\vec{\theta})\cdot\vec{\mathcal{E}}^{ext}(\vec{\theta}, \omega) \tag{7}$$

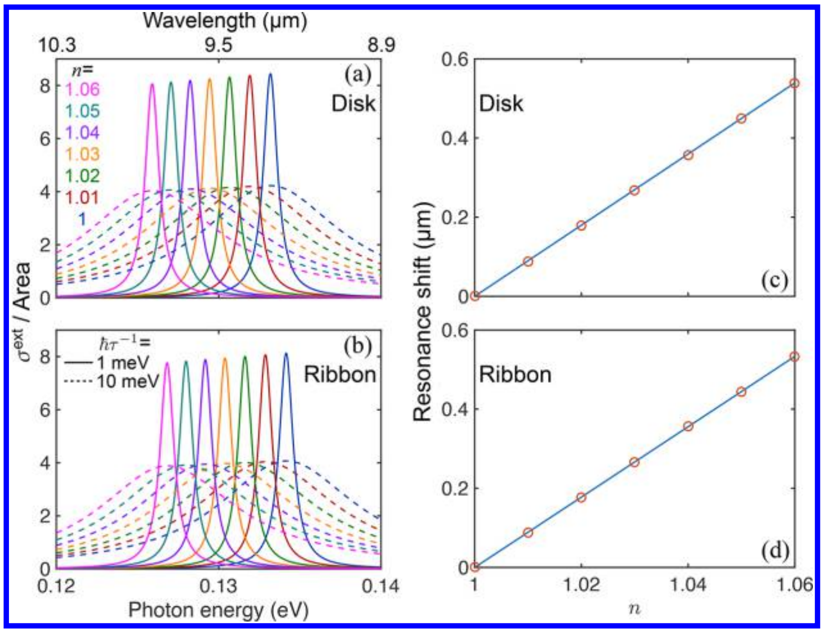

Figure 6. Refractive index sensing using individual graphene islands. (a, b) Extinction spectra of a graphene disk (D = 120 nm, panel (a)) and ribbon (D = 125 nm, panel (b)) doped at E_F = 0.35 eV for different values of the refractive index $n = \epsilon^{1/2}$ of the surrounding material (see labels). We present results for two different values of the inelastic damping rate ($\hbar\tau^{-1}$ = 1 meV, $\tau \approx 0.66$ ps, solid curves; and $\hbar\tau^{-1}$ = 10 meV, $\tau \approx 66$ fs, broken curves). (c, d) Dependence of the resonance shifts on the refractive index. Symbols correspond to the resonance positions extracted from the extinction spectra shown in panels (a) and (b). Solid curves present a linear fit, the slope of which is around 9 μm/RIU for both cases. Here, we adopt a local-RPA model for the graphene conductivity. The light incidence conditions are the same as in Figure 1.

From the closure relation, we have $\vec{\mathcal{E}}^{\rm ext}(\vec{\theta}, \omega) = \sum_j C_j\, \vec{\mathcal{E}}_j(\vec{\theta})$, which allows us to expresss the induced field as

$$\vec{\mathcal{E}}^{\rm ind}(\vec{\theta}, \omega) = \sum_j \frac{C_j}{\eta_j/\eta(\omega) - 1} \vec{\mathcal{E}}_j(\vec{\theta})$$

We now define the PWF

$$\rho_j(\vec{\theta}) \equiv \nabla_{\vec{\theta}} \cdot \sqrt{f(\vec{\theta})}\; \vec{\mathcal{E}}_j(\vec{\theta}) \tag{8}$$

which corresponds to the induced charge distribution of the plasmon eigenmode j. From eqs 5 and 6, the PWFs are found to satisfy the orthonormality condition

$$\int d^2\vec{\theta} \int d^2\vec{\theta}' \frac{\rho_j(\vec{\theta})\rho_{j'}(\vec{\theta}')}{|\vec{\theta} - \vec{\theta}'|} = -\frac{\delta_{jj'}}{\eta_j}$$

Using the continuity equation along with eq 3, we can write the induced charge density $\rho^{\rm ind}$ as

$$\rho^{\rm ind}(\vec{\theta}, \omega) = \frac{\epsilon}{D} \sum_j \frac{C_j}{1/\eta_j - 1/\eta(\omega)} \rho_j(\vec{\theta}) \tag{9}$$

Now, for a uniform electric field $\mathbf{E}^{\rm ext}$ associated with a light plane wave that acts on the graphene structure (we restate that D is small compared with the light wavelength, so we can neglect the propagation phase in the incident field), we find, upon integration of eq 7 by parts, $C_j = -D\vec{\zeta}_j \cdot \mathbf{E}^{\rm ext}$, where

$$\vec{\zeta}_j = \int d^2\vec{\theta}\; \rho_j(\vec{\theta})\vec{\theta} \tag{10}$$

is a parameter that plays the role of the mode dipole moment. From the induced charge density, we calculate the induced dipole moment as

$$\mathbf{p}^{\rm ind}(\omega) = D^3 \int d^2\vec{\theta}\; \rho^{\rm ind}(\vec{\theta}, \omega)\vec{\theta}$$

while comparing the above expression with the definition of the polarizability $\mathbf{p}^{\rm ind}(\omega) = \alpha(\omega)\cdot\mathbf{E}^{\rm ext}$, and using eq 9, we obtain the 2 × 2 in-plane polarizability tensor $\alpha(\omega)$,

$$\alpha(\omega) = \epsilon D^3 \sum_j \frac{\vec{\zeta}_j \otimes \vec{\zeta}_j}{1/\eta(\omega) - 1/\eta_j} \tag{11}$$

Finally, we calculate the extinction cross-section from the polarizability using the expression

$$\sigma^{\rm ext}(\omega) = \frac{4\pi\omega}{c\sqrt{\epsilon}} {\rm Im}\{\alpha(\omega)\}$$

In summary, eqs 8, 10, and 11 allow us to calculate the far-field scattering properties of a graphene structure from the knowledge of its PWFs.

Decay-Rate Enhancement. The decay rate Γ of an optical quantum emitter characterized by a transition dipole $\mathbf{p}^{\rm ext}$ emitting at frequency ω and located at the position $\mathbf{r}$ in an inhomogeneous space (e.g., in the presence of a graphene nanostructure) is given by[44]

$$\Gamma = \Gamma_0 + \frac{2}{\hbar} {\rm Im}\{(\mathbf{p}^{\rm ext})^* \cdot \mathbf{E}^{\rm ind}\}$$

where $\Gamma_0 = 4\omega^3|\mathbf{p}^{\rm ext}|^2/3c^3\hbar$ is the dipole decay rate in free space. We evaluate this expression in the presence of a graphene island by integrating the induced charge (eq 9) weighted by the Coulomb interaction to yield the induced electric field

$$\mathbf{E}^{\rm ind}(\mathbf{r}, \omega) = -\nabla_{\mathbf{r}} \int d^2\mathbf{R}' \frac{\rho^{\rm ind}(\mathbf{R}', \omega)}{|\mathbf{r} - \mathbf{R}'|}$$

evaluated from the PWFs defined on the graphene island.

Interaction between Islands. We consider a system composed of multiple graphene structures, indexed by n and centered at the positions $\mathbf{r}_n$. We now define $\vec{\theta} \equiv (\mathbf{r}_\parallel - \mathbf{r}_n)/D_n$, where $\mathbf{r}_\parallel$ indicates the in-plane position vector of the corresponding island and D_n is a characteristic island-dependent normalization length. We also define the eigenvalue η_{nj}, eigenmode $\vec{\mathcal{E}}_{nj}$, PWF ρ_{nj}, and mode dipole moment $\vec{\zeta}_{nj}$ for the plasmon mode j associated with the corresponding graphene island n. Then, the self-consistent induced charge density $\rho^{\rm ind}(\vec{\theta},\omega)$, having contributions from each island n, can be expressed as $\rho^{\rm ind}(\vec{\theta},\omega) = \sum_{nj} a_{nj}(\omega)\rho_{nj}(\vec{\theta})$. Note that $\vec{\theta}$ is a global 2D variable that runs over the surfaces of all of the islands and it is normalized within each of them to the corresponding size length D_n. From eqs 7–9, adding the field induced by other islands $n' \neq n$ to the external field experienced by each island n, we obtain the self-consistent expression

$$a_{nj}(\omega) = \frac{\epsilon}{D_n}\left[\frac{1}{1/\eta_{nj} - 1/\eta^{(n)}(\omega)}\right] \times \left[C_{nj} + \sum_{n' \neq n}\sum_{j'} V_{nj,n'j'} a_{n'j'}(\omega)\right]$$

for the expansion coefficients $a_{nj}(\omega)$, where $C_{nj} = -D_n\vec{\zeta}_{nj}\cdot\mathbf{E}^{\rm ext}$ and $\eta^{(n)}(\omega) = {\rm i}\sigma^{(n)}(\omega)/(D_n\omega\epsilon)$ is defined based upon the conductivity $\sigma^{(n)}(\omega)$ of island n. Here,

$$V_{nj,n'j'} = \frac{D_{n'}^2}{\epsilon}\int_n {\rm d}^2\vec{\theta}\int_{n'} {\rm d}^2\vec{\theta}' \frac{\rho_{nj}(\vec{\theta})\,\rho_{n'j'}(\vec{\theta}')}{|D_n\vec{\theta} - D_{n'}\vec{\theta}' + \mathbf{d}_{nn'}|}$$

describes the interaction between plasmon modes j and j' in two islands n and n' separated by a vector $\mathbf{d}_{nn'} = \mathbf{r}_n - \mathbf{r}_{n'}$, while integration over $\vec{\theta}$ and $\vec{\theta}'$ is restricted to the surfaces of the respective islands. After solving this linear system of equations, the total induced dipole moment can be expressed as

$$\mathbf{p}^{\rm tot} = \sum_{nj} D_n^3 a_{nj}\vec{\zeta}_{nj}$$

Eventually, the extinction cross-section of the whole system can be calculated as

$$\sigma^{\rm ext}(\omega) = \frac{4\pi\omega}{\sqrt{\epsilon}\,|\mathbf{E}^{\rm ext}|^2 c}{\rm Im}\{(\mathbf{E}^{\rm ext})^*\cdot\mathbf{p}^{\rm tot}\} \tag{12}$$

Specifically, for the analytical results shown in Figure 5, we take modes $j = 1–3$ (i.e., the PWFs displayed in Figure 3b) for each of the ribbons considered there. Incidentally, the integrals along the ribbon direction yield a logarithmic function times the infinite length of the ribbon, by which we divide the results in order to obtain a dipole per unit length.

Atomistic QM Simulations and PWFs. We adopt a previously established nearest-neighbor tight-binding model[45,46] to approximate the electronic structure of graphene islands. For a given structure, the resulting single-electron wave functions are inserted into the RPA susceptibility[47,48] to calculate its optical response.[49] To produce the results displayed in Figure 3, we have considered graphene hexagons, triangles, and ribbons that have exclusively armchair edge terminations, while the carbon sites in graphene disks and squares are arranged such that the geometry centers coincide with the center of a carbon-atom ring.

For a single graphene structure, the RPA description permits calculating the induced charge $\rho_l^{\rm ind}$ at each of its carbon atoms located at positions $\mathbf{r}_l$. Assuming that the response to an external potential $\phi^{\rm ext}$ at optical frequency ω is dominated by the plasmons of the structure with frequencies ω_j, linear response theory allows us to write the induced charge as[47]

$$\rho_l^{\rm ind} = \frac{-e^2}{\hbar}\sum_{jl'} 2\omega_j \frac{\rho_{jl}\rho_{jl'}}{\omega_j^2 - \omega(\omega + {\rm i}\tau^{-1})}\phi^{\rm ext}(\mathbf{r}_{l'})$$

where ρ_{jl} is the transition charge density (from ground state to a one-plasmon state) associated with plasmon j at the carbon atom l. For incident light with electric field $\mathbf{E}^{\rm ext}$, we have $\phi^{\rm ext}(\mathbf{r}_l) = -\mathbf{r}_l\cdot\mathbf{E}^{\rm ext}$. The set of numbers ρ_{jl} play the role of a PWF, now described in an atomistic QM fashion, and numerically obtained from the suitably normalized RPA induced charge under resonant external illumination at frequency ω_j. This concept is useful to account for the interaction between different graphene islands n, so that the effective external field experienced by each of them is the sum of the actual external field and the one produced by the rest of the islands. This idea leads to the expression

$$\rho_{nl}^{\rm ind} = \frac{-e^2}{\hbar}\sum_{jl'} 2\omega_{nj} \frac{\rho_{njl}\rho_{njl'}}{\omega_{nj}^2 - \omega(\omega + {\rm i}\tau^{-1})} \times[\phi^{\rm ext}(\mathbf{r}_{l'}) + \sum_{n'\neq n,l''} v_{nl',n'l''}\rho_{n',l''}^{\rm ind}] \tag{13}$$

where we have added labels n to denote different graphene substructures and $v_{nl,n'l'} = 1/|\mathbf{r}_{nl} - \mathbf{r}_{n'l'}|$ is the Coulomb interaction. For parallel ribbons under transversal polarization (Figure 4), $\rho_{nl}^{\rm ind}$ is repeated over all unit cells of each of the structures, so we need to sum $v_{nl,n'l'}$ over cells and restrict l and l' to the first unit cell in eq 13. Because the total induced charge per cell is zero, we subtract the $1/r$ divergent part of the Coulomb interaction (independent of atom position relative to the unit cell center), which does not contribute to eq 13. From this equation, we obtain the total induced dipole $\mathbf{p}^{\rm tot} = \sum_{nl}\mathbf{r}_{nl}\rho_{nl}^{\rm ind}$, and from here the extinction cross-section using eq 12.

■ AUTHOR INFORMATION

Corresponding Author

*E-mail: javier.garciadeabajo@nanophotonics.es.

ORCID

F. Javier García de Abajo: 0000-0002-4970-4565

Notes

The authors declare no competing financial interest.

■ ACKNOWLEDGMENTS

This work has been supported in part by the Spanish MINECO (MAT2014-59096-P and SEV2015-0522), the European Commission (Graphene Flagship 696656 and FP7-ICT-2013-613024-GRASP), Agència de Gestió d'Ajuts Universitaris i de Recerca (AGAUR) (2014-SGR-1400), and Fundació Privada Cellex.

■ REFERENCES

(1) Li, K. R.; Stockman, M. I.; Bergman, D. J. Self-similar chain of metal nanospheres as an efficient nanolens. *Phys. Rev. Lett.* **2003**, *91*, 227402.

(2) Kneipp, K.; Wang, Y.; Kneipp, H.; Perelman, L. T.; Itzkan, I.; Dasari, R. R.; Feld, M. S. Single molecule detection using surface-enhanced Raman scattering (SERS). *Phys. Rev. Lett.* **1997**, *78*, 1667–1670.

(3) Nie, S.; Emory, S. R. Probing single molecules and single nanoparticles by surface-enhanced Raman scattering. *Science* **1997**, *275*, 1102–1106.

(4) Xu, H.; Bjerneld, E. J.; Käll, M.; Börjesson, L. Spectroscopy of single hemoglobin molecules by surface enhanced Raman scattering. *Phys. Rev. Lett.* **1999**, *83*, 4357–4360.

(5) Moskovits, M. Surface-enhanced Raman spectroscopy: a brief retrospective. *J. Raman Spectrosc.* **2005**, *36*, 485–496.

(6) Yu, R.; Mazumder, P.; Borrelli, N. F.; Carrilero, A.; Ghosh, D. S.; Maniyara, R. A.; Baker, D.; García de Abajo, F. J.; Pruneri, V. Structural coloring of glass using dewetted nanoparticles and ultrathin films of metals. *ACS Photonics* **2016**, *3*, 1194–1201.

(7) Danckwerts, M.; Novotny, L. Optical frequency mixing at coupled gold nanoparticles. *Phys. Rev. Lett.* **2007**, *98*, 026104.

(8) Palomba, S.; Novotny, L. Nonlinear Excitation of Surface Plasmon Polaritons by Four-Wave Mixing. *Phys. Rev. Lett.* **2008**, *101*, 056802.

(9) Seh, Z. W.; Liu, S.; Low, M.; Zhang, S.-Y.; Liu, Z.; Mlayah, A.; Han, M.-Y. Janus Au-TiO_2 Photocatalysts with Strong Localization of Plasmonic Near-Fields for Efficient Visible-Light Hydrogen Generation. *Adv. Mater.* **2012**, *24*, 2310–2314.

(10) Gu, J.; Zhang, Y.-W.; Tao, F. Shape control of bimetallic nanocatalysts through well-designed colloidal chemistry approaches. *Chem. Soc. Rev.* **2012**, *41*, 8050.

(11) Mukherjee, S.; Libisch, F.; Large, N.; Neumann, O.; Brown, L. V.; Cheng, J.; Lassiter, J. B.; Carter, E. A.; Nordlander, P.; Halas, N. J. Hot Electrons Do the Impossible: Plasmon-Induced Dissociation of H_2 on Au. *Nano Lett.* **2013**, *13*, 240–247.

(12) Mubeen, S.; Lee, J.; Singh, N.; Kramer, S.; Stucky, G. D.; Moskovits, M. An autonomous photosynthetic device in which all charge carriers derive from surface plasmons. *Nat. Nanotechnol.* **2013**, *8*, 247–251.

(13) Clavero, C. Plasmon-Induced Hot-Electron Generation at Nanoparticle/Metal-Oxide Interfaces for Photovoltaic and Photocatalytic Devices. *Nat. Photonics* **2014**, *8*, 95–103.

(14) Mukherjee, S.; Zhou, L.; Goodman, A. M.; Large, N.; Ayala-Orozco, C.; Zhang, Y.; Nordlander, P.; Halas, N. J. Hot-Electron-Induced Dissociation of H_2 on Gold Nanoparticles Supported on SiO_2. *J. Am. Chem. Soc.* **2014**, *136*, 64–67.

(15) Qian, X.; Peng, X.-H.; Ansari, D. O.; Yin-Goen, Q.; Chen, G. Z.; Shin, D. M.; Yang, L.; Young, A. N.; Wang, M. D.; Nie, S. In vivo tumor targeting and spectroscopic detection with surface-enhanced Raman nanoparticle tags. *Nat. Biotechnol.* **2008**, *26*, 83–90.

(16) Hirsch, L.; Stafford, R.; Bankson, J.; Sershen, S.; Rivera, B.; Price, R.; Hazle, J.; Halas, N.; West, J. Nanoshell-mediated near-infrared thermal therapy of tumors under magnetic resonance guidance. *Proc. Natl. Acad. Sci. U. S. A.* **2003**, *100*, 13549–13554.

(17) Johnson, P. B.; Christy, R. W. Optical constants of the noble metals. *Phys. Rev. B* **1972**, *6*, 4370–4379.

(18) Wunsch, B.; Stauber, T.; Sols, F.; Guinea, F. Dynamical polarization of graphene at finite doping. *New J. Phys.* **2006**, *8*, 318.

(19) Hwang, E. H.; Das Sarma, S. Dielectric function, screening, and plasmons in two-dimensional graphene. *Phys. Rev. B: Condens. Matter Mater. Phys.* **2007**, *75*, 205418.

(20) Jablan, M.; Buljan, H.; Soljačić, M. Plasmonics in graphene at infrared frequencies. *Phys. Rev. B: Condens. Matter Mater. Phys.* **2009**, *80*, 245435.

(21) Ju, L.; Geng, B.; Horng, J.; Girit, C.; Martin, M.; Hao, Z.; Bechtel, H. A.; Liang, X.; Zettl, A.; Shen, Y. R.; et al. Graphene plasmonics for tunable terahertz metamaterials. *Nat. Nanotechnol.* **2011**, *6*, 630–634.

(22) Fei, Z.; Andreev, G. O.; Bao, W.; Zhang, L. M.; McLeod, A. S.; Wang, C.; Stewart, M. K.; Zhao, Z.; Dominguez, G.; Thiemens, M.; et al. Infrared nanoscopy of Dirac plasmons at the graphene-SiO_2 interface. *Nano Lett.* **2011**, *11*, 4701–4705.

(23) Shin, S. Y.; Kim, N. D.; Kim, J. G.; Kim, K. S.; Noh, D. Y.; Kim, K. S.; Chung, J. W. Control of the π plasmon in a single layer graphene by charge doping. *Appl. Phys. Lett.* **2011**, *99*, 082110.

(24) Chen, J.; Badioli, M.; Alonso-González, P.; Thongrattanasiri, S.; Huth, F.; Osmond, J.; Spasenović, M.; Centeno, A.; Pesquera, A.; Godignon, P.; et al. Optical nano-imaging of gate-tunable graphene plasmons. *Nature* **2012**, *487*, 77–81.

(25) Fei, Z.; Rodin, A. S.; Andreev, G. O.; Bao, W.; McLeod, A. S.; Wagner, M.; Zhang, L. M.; Zhao, Z.; Thiemens, M.; Dominguez, G. Gate-tuning of graphene plasmons revealed by infrared nano-imaging. *Nature* **2012**, *487*, 82–85.

(26) Yan, H.; Li, X.; Chandra, B.; Tulevski, G.; Wu, Y.; Freitag, M.; Zhu, W.; Avouris, P.; Xia, F. Tunable infrared plasmonic devices using graphene/insulator stacks. *Nat. Nanotechnol.* **2012**, *7*, 330–334.

(27) Yan, H.; Li, Z.; Li, X.; Zhu, W.; Avouris, P.; Xia, F. Infrared spectroscopy of tunable Dirac terahertz magneto-plasmons in graphene. *Nano Lett.* **2012**, *12*, 3766–3771.

(28) Fang, Z.; Thongrattanasiri, S.; Schlather, A.; Liu, Z.; Ma, L.; Wang, Y.; Ajayan, P. M.; Nordlander, P.; Halas, N. J.; García de Abajo, F. J. Gated tunability and hybridization of localized plasmons in nanostructured graphene. *ACS Nano* **2013**, *7*, 2388–2395.

(29) Brar, V. W.; Jang, M. S.; Sherrott, M.; Lopez, J. J.; Atwater, H. A. Highly confined tunable mid-infrared plasmonics in graphene nanoresonators. *Nano Lett.* **2013**, *13*, 2541–2547.

(30) Yan, H.; Low, T.; Zhu, W.; Wu, Y.; Freitag, M.; Li, X.; Guinea, F.; Avouris, P.; Xia, F. Damping pathways of mid-infrared plasmons in graphene nanostructures. *Nat. Photonics* **2013**, *7*, 394–399.

(31) Yu, R.; Alaee, R.; Lederer, F.; Rockstuhl, C. Manipulating the interaction between localized and delocalized surface plasmon-polaritons in graphene. *Phys. Rev. B: Condens. Matter Mater. Phys.* **2014**, *90*, 085409.

(32) Woessner, A.; Lundeberg, M. B.; Gao, Y.; Principi, A.; Alonso-González, P.; Carrega, M.; Watanabe, K.; Taniguchi, T.; Vignale, G.; Polini, M.; et al. Highly confined low-loss plasmons in graphene-boron nitride heterostructures. *Nat. Mater.* **2015**, *14*, 421–425.

(33) Rodrigo, D.; Limaj, O.; Janner, D.; Etezadi, D.; García de Abajo, F. J.; Pruneri, V.; Altug, H. Mid-infrared plasmonic biosensing with graphene. *Science* **2015**, *349*, 165–168.

(34) Yu, R.; Pruneri, V.; García de Abajo, F. J. Active modulation of visible light with graphene-loaded ultrathin metal plasmonic antennas. *Sci. Rep.* **2016**, *6*, 32144.

(35) García de Abajo, F. J. Multiple Excitation of Confined Graphene Plasmons by Single Free Electrons. *ACS Nano* **2013**, *7*, 11409–11419.

(36) García de Abajo, F. J. Graphene plasmonics: Challenges and opportunities. *ACS Photonics* **2014**, *1*, 135–152.

(37) Silveiro, I.; Plaza Ortega, J. M.; García de Abajo, F. J. Plasmon wave function of graphene nanoribbons. *New J. Phys.* **2015**, *17*, 083013.

(38) Zhang, S.; Genov, D. A.; Wang, Y.; Liu, M.; Zhang, X. Plasmon-induced transparency in metamaterials. *Phys. Rev. Lett.* **2008**, *101*, 047401.

(39) Wang, L.; Cai, W.; Luo, W.; Ma, Z.; Du, C.; Zhang, X.; Xu, J. Mid-infrared plasmon induced transparency in heterogeneous graphene ribbon pairs. *Opt. Express* **2014**, *22*, 32450–32456.

(40) Wenger, T.; Viola, G.; Kinaret, J.; Fogelström, M.; Tassin, P. High-sensitivity plasmonic refractive index sensing using graphene. *2D Mater.* **2017**, *4*, 025103.

(41) Li, J.; Ye, J.; Chen, C.; Li, Y.; Verellen, N.; Moshchalkov, V. V.; Lagae, L.; Van Dorpe, P. Revisiting the surface sensitivity of nanoplasmonic biosensors. *ACS Photonics* **2015**, *2*, 425–431.

(42) Gusynin, V. P.; Sharapov, S. G.; Carbotte, J. P. On the universal ac optical background in graphene. *New J. Phys.* **2009**, *11*, 095013.

(43) Yu, R.; Manjavacas, A.; García de Abajo, F. J. Ultrafast radiative heat transfer. *Nat. Commun.* **2017**, *8*, 2.

(44) Novotny, L.; Hecht, B. *Principles of Nano-Optics*; Cambridge University Press: New York, 2006.

(45) Wallace, P. R. The band theory of graphite. *Phys. Rev.* **1947**, *71*, 622–634.

(46) Castro Neto, A. H.; Guinea, F.; Peres, N. M. R.; Novoselov, K. S.; Geim, A. K. The electronic properties of graphene. *Rev. Mod. Phys.* **2009**, *81*, 109−162.

(47) Pines, D.; Nozières, P. *The Theory of Quantum Liquids*; W. A. Benjamin, Inc.: New York, 1966.

(48) Hedin, L.; Lundqvist, S. In *Solid State Physics*; Frederick Seitz, D. T., Ehrenreich, H., Eds.; Solid State Physics; Academic Press, 1970; Vol. *23*, pp 1−181.

(49) Thongrattanasiri, S.; Manjavacas, A.; García de Abajo, F. J. Quantum finite-size effects in graphene plasmons. *ACS Nano* **2012**, *6*, 1766−1775.